

CERN LIBRARIES, GENEVA

NIZATION FOR NUCLEAR RESEARCH



CM-P00063951

PRODUCTION OF HIGH TRANSVERSE MOMENTUM
LOW-MASS ELECTRON-POSITRON PAIRS
IN HIGH-ENERGY pp COLLISIONS

A. Chilingarov^{*)}, A.G. Clark, P. Darriulat, K. Eggert^{**)},
 V. Hungerbühler, P.M. Patel^{***)}, J. Strauss^{†)}, K. Zalewski^{††)} and A. Zallo

CERN, Geneva, Switzerland

M. Banner, T. Modis^{†††)}, P. Perez, J. Teiger, C. Tur,
 J.P. Vialle^{×)}, H. Zaccone and A. Zylberstejn

CEN, Saclay, France

P. Jenni, P. Strolin and G.J. Tarnopolsky

ETH, Zurich^{××)}, Switzerland

ABSTRACT

The production of electron-positron pairs of masses below $1200 \text{ MeV}/c^2$ and of transverse momentum above $1.8 \text{ GeV}/c$ has been studied in pp collisions at $\sqrt{s} = 53$ and 63 GeV . The cross-sections for ρ , ω , and ϕ production are presented. The continuum below $600 \text{ MeV}/c^2$ is consistent with origination from Dalitz decays of η and ω mesons and from semi-leptonic decays of D and \bar{D} mesons.

Geneva - 13 November 1978

(Submitted to Nuclear Physics B)

-
- *) Visitor from the Institute of Nuclear Physics, Novosibirsk, USSR.
 - **) III. Physikalisches Institut der Technischen Hochschule, Aachen, Germany.
 - ***) Visitor from McGill University, Montreal, Canada.
 - †) Institut für Hochenergie Physik der Österr. Akademie der Wissenschaften, Vienna, Austria.
 - ††) Visitor from the Institute of Nuclear Research, Krakow, Poland.
 - †††) Now at Université de Genève, Geneva, Switzerland.
 - ×) LAL, Orsay, France.
 - ××) Supported in part by the Swiss National Science Foundation.

1. INTRODUCTION

The study of lepton-pair production in hadron-hadron collisions provides a clear means of detecting vector mesons and may yield important information on charmed meson production. It requires a detector having a highly selective trigger on electrons, a good rejection against hadrons, and a large acceptance. The present results have been obtained at the CERN ISR with a double-arm spectrometer which fulfills these requirements. The spectrometer arms are located one on each side of the colliding beams, at 90° mean production angle. Air-filled Čerenkov counters and lead-glass detectors are used to identify electrons; hadron pairs are rejected to a level of 10^6 to 10^8 . Data using the same detector have previously been reported on large-mass electron-positron pairs [1] and on electron-muon coincidences [2].

In the present work we study electron-positron pairs detected in the same spectrometer arm, which results in pair masses ranging between 100 and 1200 MeV/c² and pair transverse momenta exceeding 1.8 GeV/c. Data have been collected at centre-of-mass energies of $\sqrt{s} = 53$ and 63 GeV for an integrated luminosity of $2.8 \times 10^{37} \text{ cm}^{-2}$.

2. APPARATUS

The apparatus, shown in Fig. 1, consists of two spectrometers, one on each side of the intersecting beams. Each spectrometer consists of a large-aperture magnet equipped with two sets of drift chambers (front and back) for direction and momentum measurement. The magnets are located as close as possible to the ISR vacuum pipe in order to cover a large solid angle (0.7 sr, with 0.5 sr for the lead-glass array). To reduce beam perturbations, the magnetic fields in each arm are of opposite polarity. The magnet polarities are frequently alternated to minimize experimental bias. A Čerenkov counter, located in the magnet gap, provides rejection against hadrons, both at the trigger and analysis levels. It is followed by a lead-glass array for further electron identification and electron-energy measurements. By requiring a minimum energy deposition in the lead glass and a signal in the Čerenkov counters, the trigger rate for pairs is reduced by a factor of 10^4 .

2.1 Chamber system

The momentum p of charged particles is measured from their magnetic deflection corresponding to a transverse momentum kick of 0.1 GeV/c. The lever arms for direction measurement are 19 and 40 cm in the front and back chambers, respectively. To obtain the high spatial accuracy required in the bending plane, drift chambers with a drift space of 2.5 cm are used. Shaping potential wires with 2 mm separation achieve the uniform electric field required for high-precision measurements. The sense wires are doublets with 0.5 mm separation to avoid left-right ambiguities.

The chambers have one of three possible wire orientations: parallel to the magnetic field (X) or at small angle to it (U and V). In the vertical direction, since there is no bend, the lever arm is the full spectrometer length (2 m). Therefore it is sufficient for the U and V chambers to have a small wire inclination, namely 10° in the front and 7° in the back. Such small stereo angles have the advantage of resolving ambiguities at the track reconstruction level.

The chamber arrangement can be read from Fig. 1. The front chambers (4X and 3U) have sense wires 30 cm long and are 1 m wide. The back chambers (3X, 2U, 1V on one side and 2X, 1U, 1V on the other) have sense wires 120 cm long, and are 3 m wide. The spatial separation between two signals from the same wire is limited to ~ 2 mm.

To achieve optimal spatial accuracy a large number of parameters must be determined. These include geometrical constants, an evaluation of the relationship between the track intercept and the drift time for different angles of incidence (up to 45° in these data), and a measurement of the relative delays due to different cable lengths from each wire [3]. For this purpose, data were frequently collected with the magnetic fields turned off. The effect of the magnetic field on the trajectories of the drifting electrons is significant in the last two front chambers, where it reaches 0.3 T. The corresponding correction is evaluated by comparing adjacent drift chamber cells, where the effect of the magnetic field is of opposite sign.

The chamber redundancy allows a measurement of both the spatial resolution and the track reconstruction efficiency in each set of chambers. In both the

front and back chambers a spatial resolution of $\{(150)^2 + (300 \tan \theta)^2\}^{1/2}$ μm is achieved. The observed width of the J/ψ peak is well described by this relation, once radiative losses and multiple scattering are included. For the duration of the experiment a global momentum accuracy of $\Delta p/p = 10^{-2} \{9 + (4.2p)^2\}^{1/2}$ was maintained.

The track reconstruction efficiency in each set of chambers is 97%, except for one back chamber set (2X, 1U, 1V) where it is 85% because of the lack of redundancy.

2.2 Lead-glass arrays

Each lead-glass array, located 2.3 m from the beams, consists of 138 lead-glass blocks arranged in 7 horizontal rows. Each block (15×15 cm^2 in cross-section and 14.8 radiation lengths thick) is equipped with a 5 in. phototube, shielded from the stray magnetic field by the 2 cm iron plate inserted between the E and F hodoscopes (see Section 2.4). Anode pulses are analysed in 10-bit analogue-to-digital converters, while pulses from the last dynode are added for subsequent energy discrimination.

The calibration of the energy response of the detector is of crucial importance. Before installation each block was calibrated in a 2 GeV electron beam at the CERN PS and its phototube voltage was adjusted to ensure a uniform gain over the full array. This calibration was maintained throughout the experiment by means of reference light sources (^{241}Am deposited on a small plastic scintillator which is glued to the front face of each block). To obtain a response similar to that of a 1.5 GeV photon, the anode pulses were amplified by a factor of 10 during calibration.

The energy resolution, including uncertainties on the absolute cell-to-cell calibration, is measured [4] to have the form

$$\frac{\Delta E}{E} = \left\{ (0.05)^2 + \frac{(0.12)^2}{E(\text{GeV})} \right\}^{1/2} .$$

In addition, the lead-glass arrays were periodically recessed to 4 m from the intersection, at which distance $\pi^0 \rightarrow \gamma\gamma$ decays yield two spatially resolved

photons. Data collected in this configuration enable a check of the calibration of each cell within $\pm 5\%$ for photon energies between 0.5 and 2 GeV.

The linearity of the ADCs has been measured with an electronic pulser, simulating as closely as possible the phototube response. The gains of the amplifiers were measured by a similar method. It should be noted that the gain stability of the amplifiers is more important than the absolute knowledge of the gain, because each lead-glass block is always calibrated in energy with the same amplifier.

2.3 Čerenkov counters

An air-filled Čerenkov counter is located in each magnet gap. The threshold for pion detection is 5.8 GeV/c. Each counter has 12 cells, 6 above and 6 below the medium plane. Each cell is equipped with a 5 in. phototube and with an elliptical mirror made of 6 mm thick plexiglas, the foci of which are the centre of the beam intersection and the photocathode centre. At the highest ISR luminosity the length of the interaction region (diamond) is 60 cm and one reflection on the elliptical mirror is insufficient to focus the whole diamond on the photocathode. To ensure that each cell sees the entire diamond over a certain angular range, conical light collectors are installed in front of the photocathodes (Fig. 1).

The average path length through the gas is 70 cm. The Čerenkov efficiency has been measured in special runs for which a photon converter (0.1 radiation length) was inserted in front of the first drift chamber. Converted gamma-rays were identified as being a pair of opposite sign particles with invariant mass less than $30 \text{ MeV}/c^2$ and with a total momentum in agreement with the energy deposited in the lead glass. We also ensured by simulating the light trajectories that this gamma yielded twice the light of a single electron. This was usually the case for electron energies above 300 MeV. In these conditions, the Čerenkov efficiency is measured to be $(97 \pm 1)\%$. From that we deduce a single electron efficiency of 83%, corresponding on an average to two photoelectrons.

2.4 Trigger

Three sets of scintillator hodoscopes A, E, and F (see Fig. 1) are used for the trigger. The pulse height is recorded for each counter and the time of flight between the A and E hodoscopes is measured.

For trigger purposes, the twelve Čerenkov cells of each spectrometer are grouped into four quadrants. In the same way the last dynode signals of each lead-glass cell of a same array are linearly added into four overlapping quadrants matching those of the Čerenkov counter. The E and F hodoscopes are divided into two overlapping sets matched to appropriate lead-glass quadrants. An electron trigger requires a coincidence between associated E, F, lead-glass, and Čerenkov quadrants, in addition to a signal from any A counter in the same spectrometer.

For low-mass electron pairs the coincidence of two such quadrant triggers is required, both in the same spectrometer. The lead-glass quadrant threshold is about 400 MeV. In addition, the energy deposited in the entire associated lead-glass wall is required to be above a threshold which depends on the running conditions, typically corresponding to 1.8-2.5 GeV in the centre of mass.

3. DATA REDUCTION

Owing to the small number of events, the dominant concern of the analysis is to retain as many genuine electron-positron pairs as possible, while rejecting efficiently the background. Misidentified hadrons, asymmetric Dalitz pairs, and gamma-rays converting in the vacuum pipe or the A counters contribute to the background.

Same sign electron pairs, e^+e^+ and e^-e^- , are analysed in parallel with opposite sign pairs. The expected background consists of uncorrelated pairs of either misidentified hadrons or decay- or conversion- e^\pm , contributing equally to the opposite and the same sign pairs. Thus the same sign pairs provide a monitor of the background contamination. However, fully reconstructed e^+e^- pairs from a single Dalitz decay, such as π^0 or $\eta \rightarrow \gamma e^+e^-$, do not populate the same sign sample. They are retained in the analysis and are subtracted from the final data sample.

An electron is defined as a fully reconstructed track with a signal in the Čerenkov cell through which it passes. In addition, an electron is required to deposit its energy in the lead-glass array. For this purpose, clusters are defined as sets of adjacent lead-glass cells having an energy deposition above 100 MeV [2]. When the energy distribution within a cluster peaks in two non-adjacent cells, the cluster is split into two different sub-clusters. Two

electromagnetic showers can be resolved down to a minimum separation between the electron impacts on the lead-glass array, which varies between 18 and 38 cm, depending on the energy, angle of incidence, and location with respect to the cell lattice.

Each electron must have an associated cluster of more than 500 MeV within 12.5 cm of its impact point on the lead-glass array. In addition, its momentum p , as measured from the track deflection by the magnet, has to agree with the energy deposition E in the lead glass within 2 standard deviations (momentum and energy resolutions are given in Section 2). This gives good rejection against hadrons, which typically lose only a fraction of their energy in the lead glass, and against overlaps of a photon with an electron which give $E > p$. It results in a 5% loss of genuine electrons. The requirement that each electron track has at least one hit in one of the two drift-chamber planes before the A counters removes electrons originating from γ -conversions in the A counters.

Electron pairs are now defined as two electrons detected in the same spectrometer. The sum of their energies is required to be above the lead-glass threshold in the corresponding run.

Figure 2 shows the electron-positron mass spectrum after application of all these cuts, hereafter referred to as the loose cuts. The pair mass is computed with the electron energies defined as the weighted average of E and p .

The mass region $600 < M_{ee} < 1200 \text{ MeV}/c^2$ is dominated by vector mesons (ρ , ω , ϕ). There is a background of $(17 \pm 4)\%$ left in this region. We consider this sufficiently clean for a meaningful determination of the ρ , ω , and ϕ production cross-sections (see Section 4).

In the region below $600 \text{ MeV}/c^2$, however, where most of the pairs are observed, the background is further reduced by tighter requirements on the e^+e^- vertex, by demanding that the pattern of energy deposition in the lead glass be consistent with that of a single electron and that the time of flight between the A and E counters be compatible with a $\beta = 1$ particle. In addition, events with a large number of extraneous hits in the front drift chambers near the electron tracks are eliminated.

The mass spectrum resulting from these strict cuts is shown in Fig. 3. The background is now reduced to $(5 \pm 1)\%$. The loss of genuine events is $(25 \pm 5)\%$. This can be evaluated from the data sample itself with the assumption that the number of background events among the opposite sign pairs is equal to the number of same sign events. Any excess in the loss of opposite sign pairs over same sign pairs is then due to the loss of genuine events. The effect of the strict cuts is independently evaluated on well-identified J/ψ 's and found to be compatible with a reduction of good events by 25%. Table 1 summarizes the detection efficiencies.

4. RESULTS

4.1 Inclusive vector meson production cross-sections

Eighty per cent of the data are taken at $\sqrt{s} = 53$ GeV and 20% at $\sqrt{s} = 63$ GeV. Owing to the low statistics, the two data samples are added together. The loose cuts are applied to the mass range $520 < M_{ee} < 1200$ MeV/c² (Fig. 2).

The acceptance for e^+e^- pairs is computed as a function of mass and transverse momentum, and is averaged over the different running conditions. The pairs are assumed to be produced with a uniform rapidity distribution in the accepted range $|y| < 0.5$ and to decay isotropically in their rest frame.

Figure 4 shows the invariant cross-section versus p_t for e^+e^- pairs with masses between 680 and 880 MeV/c². It is assumed that all pairs originate from $\rho \rightarrow e^+e^-$. If all the events were ω 's, the cross-section would be reduced by the ratio of the branching fractions, i.e. by a factor 1.77. The shape of the p_t distribution is consistent with that of inclusive π 's. The pair acceptance as a function of M_{ee} is computed by integrating over p_t according to the parametrization of Alper et al. [4]. The results are not sensitive to the form of the parametrization, since the dominant contributions come from a rather restricted p_t range ($p_t \lesssim 2.5$ GeV/c).

The acceptance for e^+e^- pairs has a p_t threshold which is an increasing function of the pair mass, owing to the aperture of the detector. To avoid biases near the p_t threshold, while retaining a maximum of events, a mass-dependent cut

$p_t > 1.6 + 0.5 M_{ee}$ GeV/c is introduced, where M_{ee} is in GeV/c². Figure 5 shows the inclusive production cross-section for e^+e^- pairs with $p_t > 1.6 + 0.5 M_{ee}$ GeV/c at $y = 0$, together with the acceptance as a function of the pair mass (Table 2).

A fit is made to the form:

$$\left. \frac{d^2\sigma}{dMdy} \right|_{y=0} = a_{\rho+\omega} f(M,r,\alpha) + a_\phi \phi(M) + b + cM,$$

where $\phi(M)$ is the expected mass distribution of the ϕ , normalized to one, after energy resolution smearing and bremsstrahlung are taken into account; $f(M,r,\alpha)$ is the mass distribution of the interfering ρ and ω ,

$$f(M,r,\alpha) = \frac{1}{2\pi} \left| \frac{\sqrt{r}\Gamma_\rho}{M - M_\rho + i\Gamma_\rho/2} + \frac{\sqrt{(1-r)}\Gamma_\omega e^{i\alpha}}{M - M_\omega + i\Gamma_\omega/2} \right|^2,$$

modified by experimental effects, and r is the ratio of the number of e^+e^- pairs attributed to the ρ to the total number of e^+e^- from ω and ρ . For pure ρ or ω ($r = 1$ or 0), $f(M,r,\alpha)$ is normalized to one, but not in general. The linear term, $b + cM$, is expected to account for the 17% background in the data sample and continuum contributions.

The resonance widths are kept fixed at their established values, but their masses are left free to account for possible small errors in the spectrometer calibration, except for $M_\omega = M_\rho + 10$ MeV/c². The data show a rather narrow peak near the ρ - ω mass, compatible with pure ω production. If r is left free, but constrained to be positive, the fit yields $r = 0$ with a $\chi^2 = 11.6$ for 8 degrees of freedom. However, the fit is not very sensitive to the relative fraction of ρ and ω production, because the mass resolution of 35 MeV/c² is considerably larger than the ω width. In order to determine how much ρ contribution is allowed by the data, fits were made for different values of r (Table 3). There is still an acceptable χ^2 of 13.6 for 9 degrees of freedom when equal ρ and ω production cross-sections are imposed ($r = 0.36$).

The sum of the ρ and ω contributions is almost independent of r , so that

$$B \left. \frac{d\sigma}{dy} \right|_{y=0}^{\rho \rightarrow e^+e^-} + B \left. \frac{d\sigma}{dy} \right|_{y=0}^{\omega \rightarrow e^+e^-} = (1.98 \pm 0.49) \times 10^{-33} \text{ cm}^2 \quad \text{for } p_t > 2.0 \text{ GeV}/c$$

$$B \left. \frac{d\sigma}{dy} \right|_{y=0}^{\phi \rightarrow e^+e^-} = (0.83 \pm 0.36) \times 10^{-33} \text{ cm}^2 \quad \text{for } p_t > 2.1 \text{ GeV}/c .$$

The uncertainties of the detection efficiency and the luminosity measurement are included in the error.

In the following, we *assume* equal ρ and ω cross-sections. The branching ratios may then be inserted to obtain

$$\left. \frac{d\sigma}{dy} \right|_{y=0}^{\rho^0} = \left. \frac{d\sigma}{dy} \right|_{y=0}^{\omega} = (0.17 \pm 0.06) \times 10^{-28} \text{ cm}^2 \quad \text{for } p_t > 2.0 \text{ GeV}/c$$

$$\left. \frac{d\sigma}{dy} \right|_{y=0}^{\phi} = (0.27 \pm 0.12) \times 10^{-29} \text{ cm}^2 \quad \text{for } p_t > 2.1 \text{ GeV}/c .$$

For comparison, the average of the inclusive π^+ and π^- production cross-sections [4] at $\sqrt{s} = 53 \text{ GeV}$ is

$$\left. \frac{d\sigma}{dy} \right|_{y=0}^{\frac{1}{2}(\pi^+\pi^-)} = \begin{array}{l} 0.29 \times 10^{-28} \text{ cm}^2 \quad \text{for } p_t > 2.0 \text{ GeV}/c \\ 0.22 \times 10^{-28} \text{ cm}^2 \quad \text{for } p_t > 2.1 \text{ GeV}/c . \end{array}$$

Thus the ratios of the vector meson to π^0 production near $p_t = 2.2 \text{ GeV}/c$ are

$$\left. \left(\frac{d\sigma}{dy} \right)_{\rho} \right/ \left. \left(\frac{d\sigma}{dy} \right)_{\pi} \right|_{y=0} = \left. \left(\frac{d\sigma}{dy} \right)_{\omega} \right/ \left. \left(\frac{d\sigma}{dy} \right)_{\pi} \right|_{y=0} = 0.58 \pm 0.19$$

$$\left. \left(\frac{d\sigma}{dy} \right)_{\phi} \right/ \left. \left(\frac{d\sigma}{dy} \right)_{\pi} \right|_{y=0} = 0.12 \pm 0.05 .$$

Previous measurements at the ISR [5] have given ρ/π ratios between 0.12 and 1 at p_t values ranging from 1 GeV/c to 3.5 GeV/c. A Fermilab experiment [6] has found a ϕ/π ratio of $4 \pm 1\%$ at $p_t = 2 \text{ GeV}/c$ and $\sqrt{s} = 28 \text{ GeV}$.

The acceptance of the apparatus distorts the angular distribution of the e^+e^- pairs and precludes any measurement of the spin alignment. If there was full alignment perpendicular to the production plane, the acceptance in the $\rho\omega$ region would decrease by 18%.

4.2 The low-mass continuum

The strict cuts are applied to the data sample (Fig. 3) in the mass range below $600 \text{ MeV}/c^2$. As the electron-positron mass drops below $300 \text{ MeV}/c^2$, it becomes increasingly difficult to compute accurately the acceptance. Low-mass pairs tend to have small opening angles; however, they are forced by the trigger to hit two different Čerenkov counters and thus to be close to the mirror edges. Therefore, the acceptance calculation becomes very sensitive to misalignment of the Čerenkov counter and effects due to light cone overlaps. We take these uncertainties into account with an additional mass-dependent normalization error, estimated from a Monte Carlo study of the mass dependence of the sensitivity to such effects, and which decreases smoothly from 30% at $60 \text{ MeV}/c^2$ to 10% at $300 \text{ MeV}/c^2$.

The contributions of the Dalitz decays of the η , ω , and η' mesons to the e^+e^- mass spectrum are computed [7], assuming a uniform rapidity distribution and the p_t distribution of π 's at the ISR [4]. Again, the result does not depend critically on the p_t parametrization. The assumptions on the production cross-sections and the decay branching ratios are summarized in Table 4. The η/π production ratio is taken from the Fermilab measurement of Donaldson et al. [8]; assuming the same value for η'/π , the η' contribution is negligible.

The ω/π ratio is taken from Section 4.1, under the assumption that the ρ and ω cross-sections are equal.

There is no appreciable contribution from known Dalitz decays to the mass region between 400 and $600 \text{ MeV}/c^2$, where there is a significant excess of events. Possible sources of these events are the semi-leptonic decays of D and \bar{D} mesons. An $e\mu$ coincidence experiment [2] at the ISR, using the same detector, indicates a $D\bar{D}$ production cross-section of $70 \pm 36 \mu\text{b}$, assuming the parametrization of Bourquin and Gaillard [9], a branching ratio of 10% for the decay of a D meson into an electron, and an equal probability for the decays $D \rightarrow K e \nu$ and $D \rightarrow K^* e \nu$. Under the same hypotheses, the resulting e^+e^- spectrum is computed. A fit is made to the background-subtracted mass distribution between 120 and $600 \text{ MeV}/c^2$, assuming

that all pairs are due to Dalitz decays and $D\bar{D}$ semi-leptonic decays. Both the mass-dependent scale errors below $300 \text{ MeV}/c^2$ and the over-all normalization uncertainty of 15% are taken into account. The results of the fit are summarized in Table 5. They indicate that the detection efficiency below $300 \text{ MeV}/c^2$ is overestimated by up to 2 standard deviations and/or the η -production cross-section is up to 20-30% lower than assumed. A $D\bar{D}$ production cross-section of $73 \pm 21 \mu\text{b}$ fits the rest of the electron-positron pairs (Fig. 5). The background below the $\rho\omega$ and the ϕ is then also mainly accounted for by pairs from $D\bar{D}$ decays. The acceptance of the apparatus does not permit a significant search for associated production of K mesons. With the previously mentioned assumptions, two $K_S^0 \rightarrow \pi^+\pi^-$ are expected and one candidate for such a decay has been observed. We emphasize that this does not constitute a measurement of the $D\bar{D}$ production cross-section.

A possible contribution to the mass region $400 < M_{ee} < 600 \text{ MeV}/c^2$ comes from the production of direct virtual photons. If, for example, 50% of the events between 200 and $600 \text{ MeV}/c^2$ are assumed to be of such origin, an extrapolation to real γ 's, according to the mass distribution $(\alpha/2\pi)(dM^2/M^2)$, results in a ratio $\gamma/\pi^0 = 1.9\%$ at $p_t = 1.9 \text{ GeV}/c$. However, it is unlikely that this contribution is dominant, since more than half of the events below $200 \text{ MeV}/c^2$ would also come from single virtual photons, implying that the detection efficiency below $300 \text{ MeV}/c^2$ and/or the η production cross-section are even lower than suggested by the fit of Table 5.

Acknowledgements

Professor B. Richter has contributed to the experiment for part of the time; we gratefully acknowledge his help and advice. The technical assistance of L. Bonnefoy, J.M. Chapuis, M. Lemoine and A. Mottet is gratefully acknowledged. We wish to thank Dr. G. Gounaris and Prof. H. Satz for useful discussions.

REFERENCES

- [1] A.G. Clark et al., Nuclear Phys. B142 (1978) 29.
- [2] A.G. Clark et al., Phys. Letters 74B (1978) 267.
- [3] P. Perez, Thèse de 3e cycle, Saclay (1978).
- [4] B. Alper et al., Nuclear Phys. B100 (1975) 237.
- [5] A.J. Lankford, CERN EP Internal Report 78-3 (1978).
P. Darriulat et al., Nuclear Phys. B107 (1976) 429.
M. Della Negra et al., Nuclear Phys. B127 (1977) 1.
M.G. Albrow et al., Studies of pp collisions at the CERN ISR with an identified
charged hadron of high transverse momentum at 90° , submitted to Nuclear
Phys. B.
- [6] C.W. Akerlof et al., Phys. Rev. Letters 39 (1977) 861.
- [7] D.W. Joseph, Nuovo Cimento 16 (1960) 997.
N. Kroll and W. Wada, Phys. Rev. 98 (1955) 1355.
- [8] G.J. Donaldson et al., Phys. Rev. Letters 40 (1978) 684.
- [9] M. Bourquin and J.M. Gaillard, Nuclear Phys. B114 (1976) 334.

Table 1

Detection efficiencies

Single electrons	0.66 ± 0.04
Pairs (loose cuts)	0.44 ± 0.055
Pairs (strict cuts)	0.33 ± 0.045

Table 2

Production cross-section for e^+e^- pairs
with $p_t > 1.6 + 0.5 M_{ee}$ GeV/c

M_{ee} [GeV/c ²]	$(d\sigma/dMdy)_{y=0}$ [in 10^{-33} cm ² /(GeV/c ²)]
0.06	216.0 ± 68.0
0.10	83.0 ± 25.0
0.14	32.0 ± 8.8
0.18	26.0 ± 6.2
0.22	15.5 ± 3.7
0.26	14.8 ± 3.2
0.30	13.5 ± 2.9
0.34	9.6 ± 2.3
0.38	9.7 ± 2.3
0.42	10.4 ± 2.5
0.46	10.0 ± 2.4
0.50	6.3 ± 1.9
0.54	7.6 ± 2.2
0.58	5.4 ± 1.7
0.62	5.7 ± 1.8
0.66	4.8 ± 1.7
0.70	8.3 ± 2.3
0.74	26.1 ± 5.3
0.78	14.5 ± 3.7
0.82	3.9 ± 1.7
0.86	5.0 ± 2.0
0.90	3.5 ± 1.8
0.94	2.0 ± 1.4
0.98	10.5 ± 3.3
1.02	6.8 ± 2.8
1.06	2.4 ± 1.7
1.10	1.3 ± 1.3
1.14	1.4 ± 1.4
1.18	1.6 ± 1.6

Table 3

Fit of the data between 520 and 1200 MeV/c² to the form

$$B \frac{d^2\sigma}{dMdy} \Big|_{y=0} = [a_{\rho+\omega} f(M, r, \alpha) + a_\phi \phi(M) + b + cM] \times 10^{-33} \text{ cm}^2 / (\text{GeV}/c^2)$$

r	$\sigma_\rho / \sigma_\omega$	χ^2 (D.F.)	Fit parameters	$B \frac{d\sigma}{dy} \Big _{y=0}$ (in 10^{-33} cm^2)
0	0	11.6 (9)	$a_{\rho+\omega} = 1.76 \pm 0.4$ $a_\phi = 0.77 \pm 0.34$ $\alpha = \text{indeterminate}$ $b = 210 \pm 72$ $c = -190 \pm 85 \text{ (GeV}/c^2)^{-1}$ $M_\rho = 0.748 \pm 0.007 \text{ GeV}/c^2$ $M_\phi = 1.014 \pm 0.013 \text{ GeV}/c^2$	$\rho + \omega = 1.76 \pm 0.45$ $\phi = 0.77 \pm 0.35$
0.36	1	13.6 (9)	$a_{\rho+\omega} = 1.53 \pm 0.42$ $a_\phi = 0.83 \pm 0.35$ $\alpha = -0.75 \pm 0.5$ $b = 202 \pm 82$ $c = -192 \pm 79 \text{ (GeV}/c^2)^{-1}$ $M_\rho = 0.743 \pm 0.008 \text{ GeV}/c^2$ $M_\phi = 1.019 \pm 0.013 \text{ GeV}/c^2$	$\rho + \omega = 1.98 \pm 0.49$ $\phi = 0.83 \pm 0.36$
0.6	2.6	15.4 (9)	$a_{\rho+\omega} = 1.70 \pm 0.46$ $a_\phi = 0.88 \pm 0.35$ $\alpha = 0.65 \pm 0.5$ $b = 168 \pm 71$ $c = -169 \pm 69 \text{ (GeV}/c^2)^{-1}$ $M_\rho = 0.743 \pm 0.008 \text{ GeV}/c^2$ $M_\phi = 1.020 \pm 0.013 \text{ GeV}/c^2$	$\rho + \omega = 2.2 \pm 0.59$ $\phi = 0.88 \pm 0.36$

Table 4

Assumptions on Dalitz contributions

Dalitz decay	Production cross-section (meson/ π^0)	Branching ratio $M \rightarrow N\gamma/M \rightarrow \text{all}$	Branching ratio $M \rightarrow Ne^+e^-/M \rightarrow \text{all}$
$\eta \rightarrow \gamma e^+e^-$	0.4	0.38 ± 0.01	0.0058 ± 0.0002
$\omega \rightarrow \pi^0 e^+e^-$	0.5	0.088 ± 0.005	0.0007 ± 0.00004
$\eta_{958} \rightarrow \gamma e^+e^-$	0.4	0.020 ± 0.003	0.00034 ± 0.00005

Table 5

Fit of the data between $120 \text{ MeV}/c^2$ and $600 \text{ MeV}/c^2$

The following form is used:

$$F(M) = \alpha[1 + \beta\sigma(M)] [D_1(M) + \gamma D_2(M)]$$

where

$D_1(M)$ = acceptance corrected contribution from Dalitz decays, computed with the assumptions of Table 4.

$D_2(M)$ = contribution from $D\bar{D}$ produced with $\sigma_{\text{tot}} = 70 \text{ } \mu\text{b}$ according to the Bourquin-Gaillard parametrization.

$\sigma(M)$ = mass-dependent normalization error, decreasing smoothly from 20% at $120 \text{ MeV}/c^2$ to 10% at $300 \text{ MeV}/c^2$.

The χ^2 is defined as

$$\chi^2 = \sum_i \frac{[N_i - F(M_i)]^2}{N_i} + \beta^2 + \frac{(1 - \alpha)^2}{\sigma_\alpha^2}$$

with σ_α = over-all normalization error = 15%.

Results:

$$\alpha = 1.03 \pm 0.11$$

$$\beta = -2.1 \pm 0.5$$

$$\gamma = 1.05 \pm 0.24$$

$$\chi^2 = 15.9 \text{ for 11 degrees of freedom.}$$

Figure captions

- Fig. 1 : Exploded view of one of the two spectrometers.
- Fig. 2 : Invariant mass distribution of e^+e^- for loose cuts (Section 3). The shaded area represents the sum of e^+e^+ and e^-e^- pairs.
- Fig. 3 : Invariant mass distribution of e^+e^- for strict cuts (Section 3). The shaded area represents the sum of e^+e^+ and e^-e^- pairs.
- Fig. 4 : The invariant production cross-section for e^+e^- pairs of $680 < M_{ee} < 880 \text{ MeV}/c^2$, at $y = 0$, as a function of p_t . The branching ratio of $\rho \rightarrow e^+e^-$ (4.3×10^{-5}) is assumed. The solid line is the π -production cross-section at $\sqrt{s} = 53 \text{ GeV}$ [4].
- Fig. 5 : The invariant mass distribution of e^+e^- , after correction for acceptance and detection efficiency. The solid line represents the acceptance, in arbitrary units, for e^+e^- pairs produced with the p_t distribution of Alper et al. [4] and decaying isotropically.
- Fig. 6 : Fit to the e^+e^- mass spectrum, assuming only contributions from Dalitz decays and $D\bar{D}$ semi-leptonic decays (solid lines). The dashed line is the sum of both contributions.

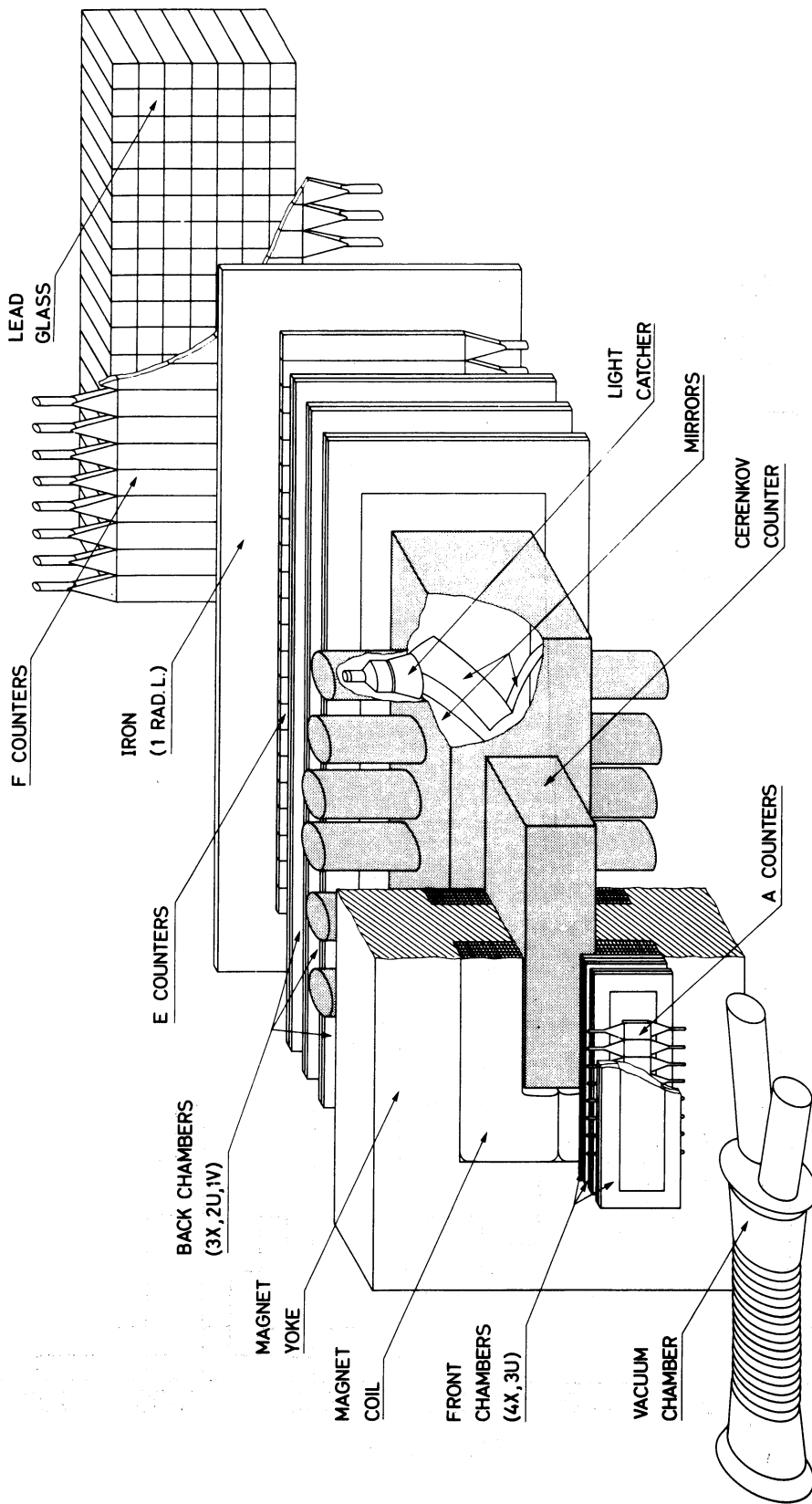


Fig. 1

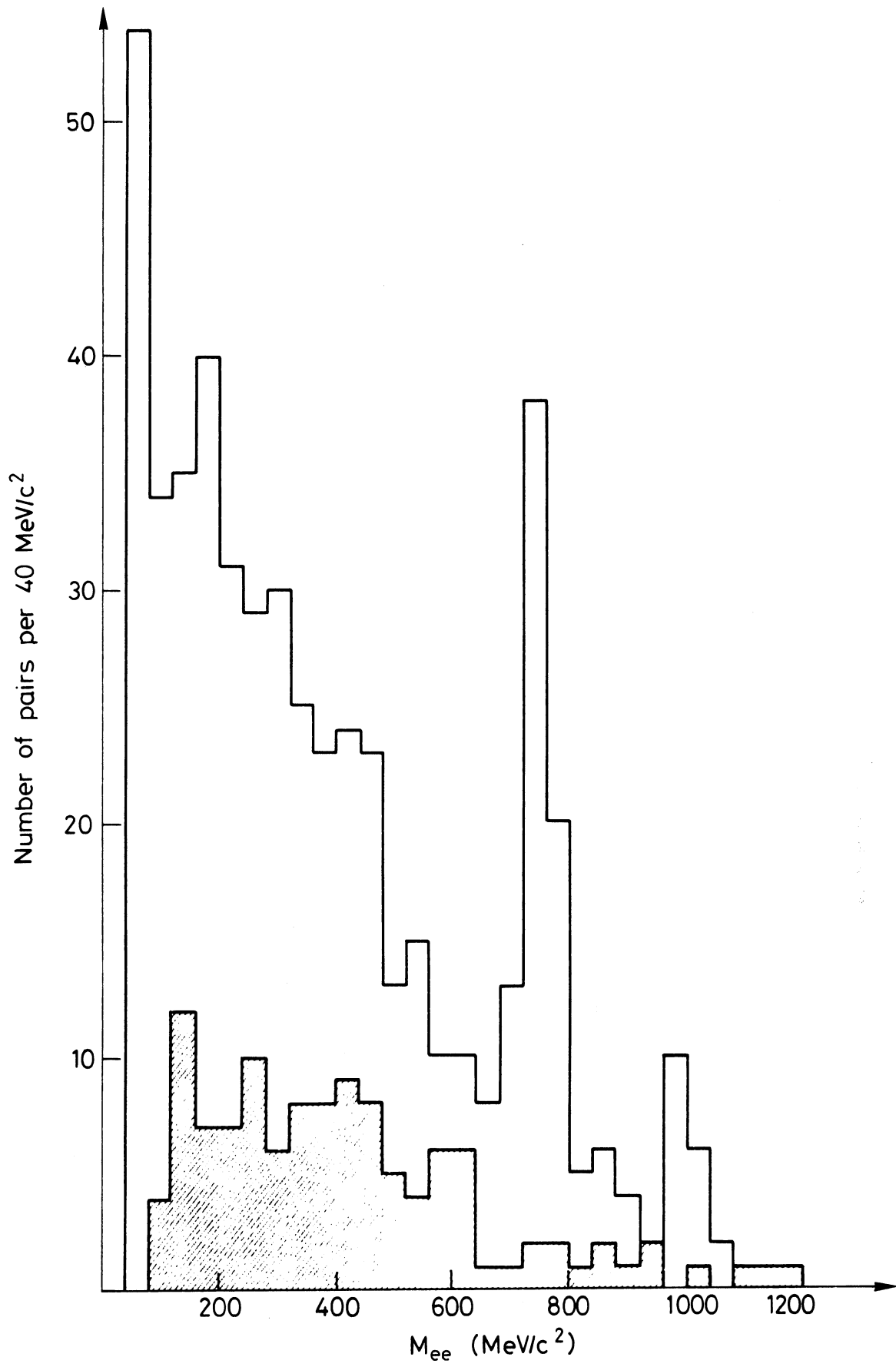


Fig. 2

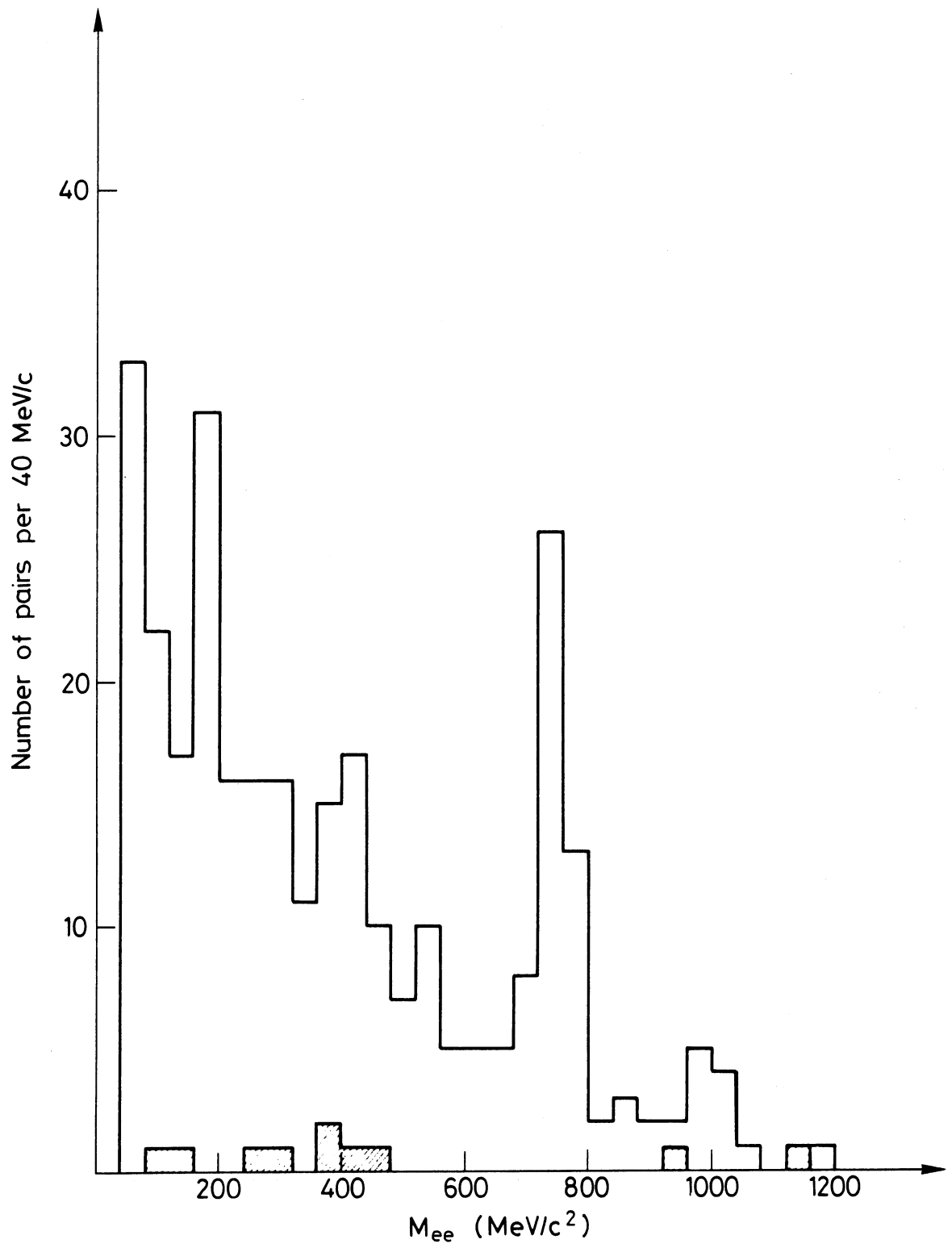


Fig. 3

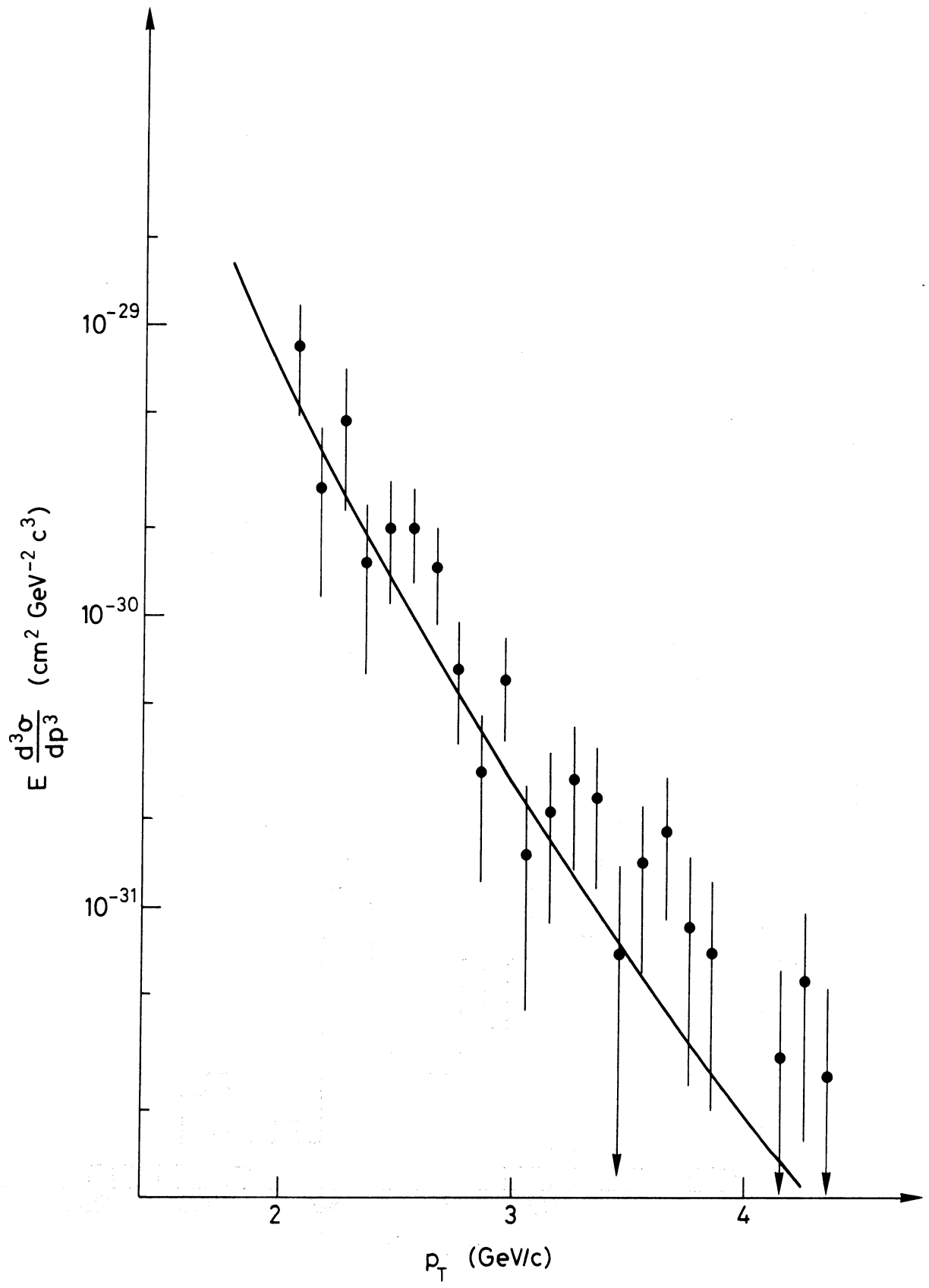


Fig. 4

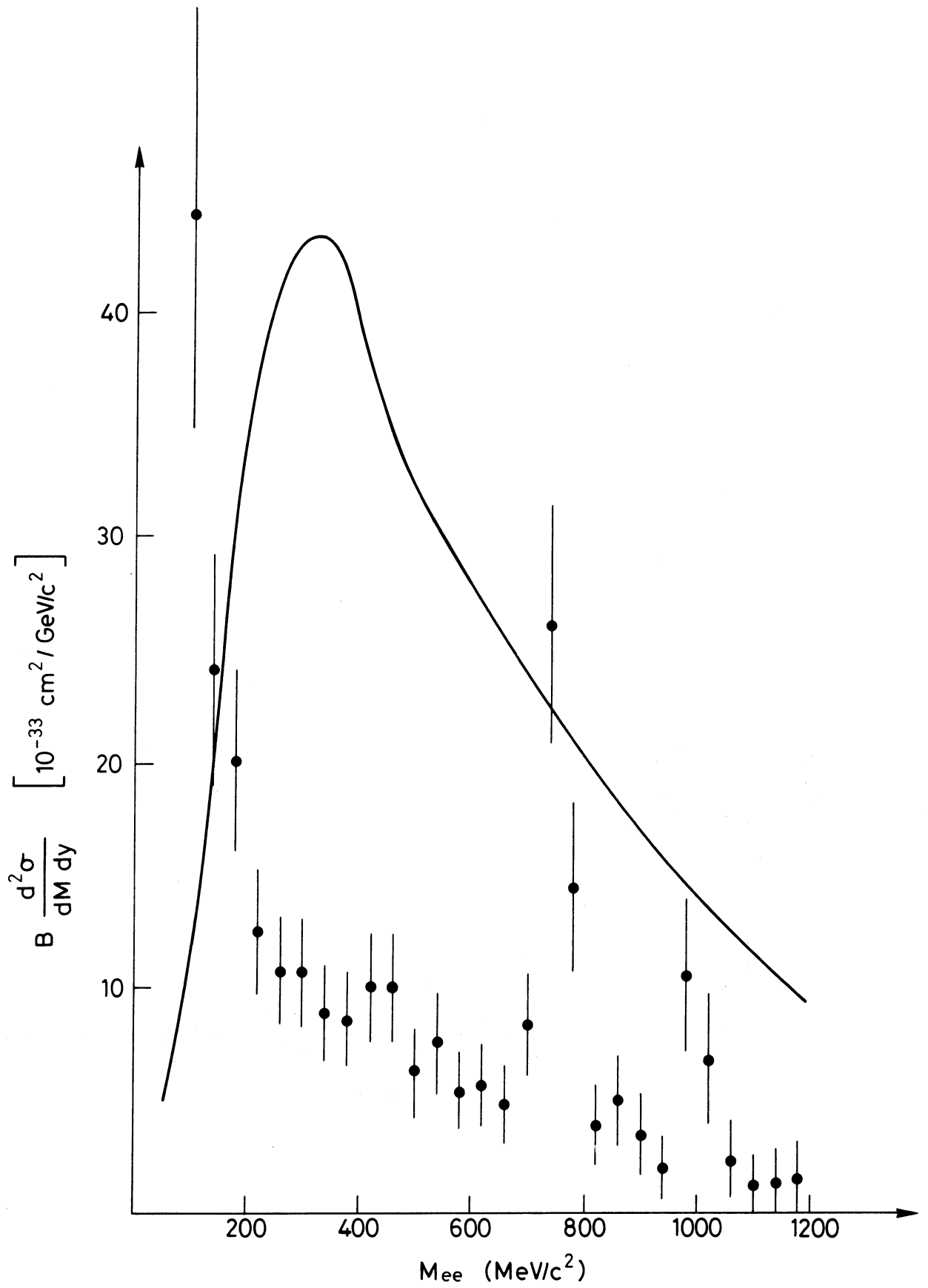


Fig. 5

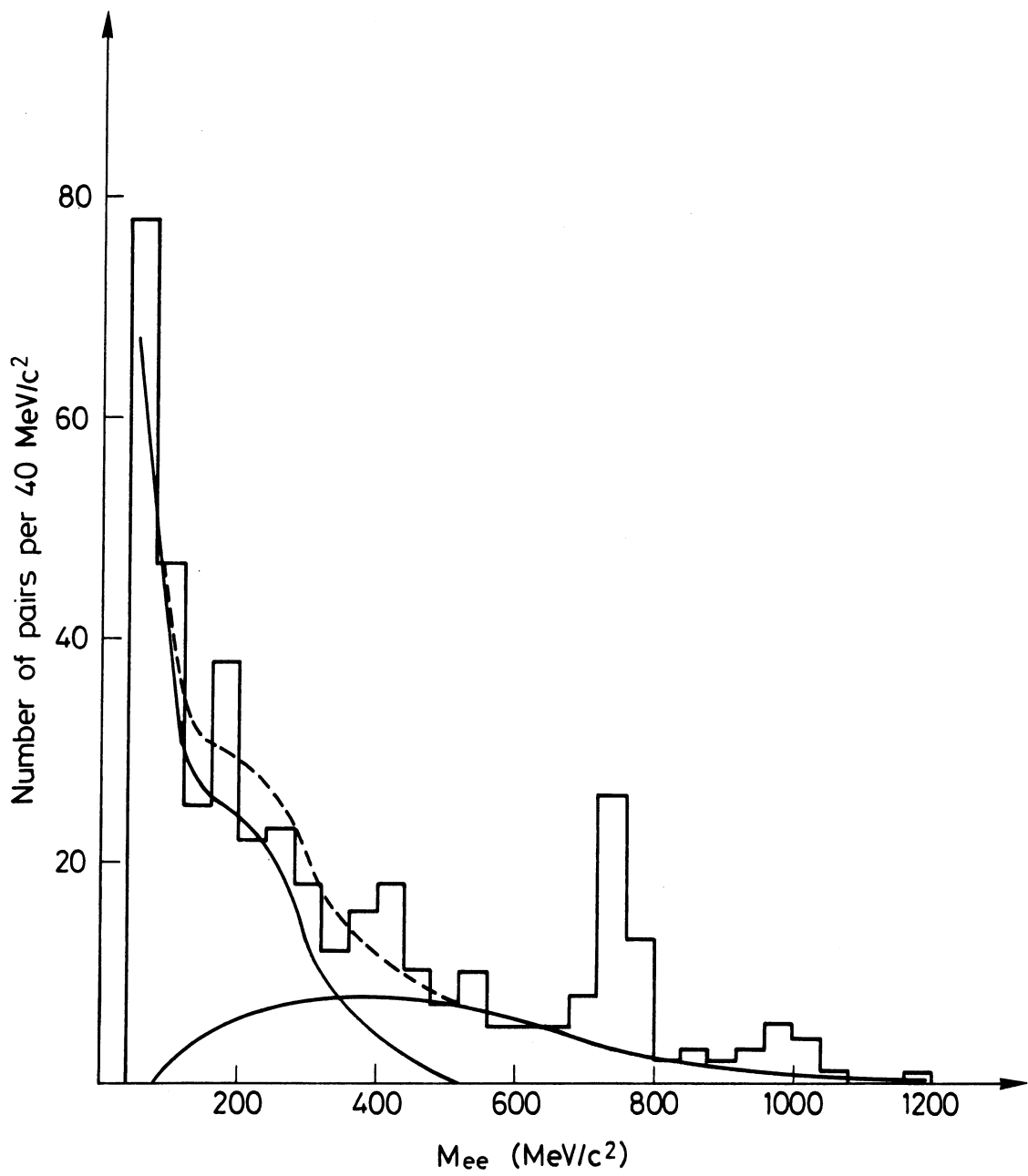


Fig. 6